ACS Catalysis

pubs.acs.org/acscatalysis Research Article

# Modeling the Mechanism of $CO_2$/Cyclohexene Oxide Copolymerization Catalyzed by Chiral Zinc $\beta$-Diiminates: Factors Affecting Reactivity and Isotacticity

Huiling Shao,* Yernaidu Reddi, and Christopher J. Cramer

Cite This: *ACS Catal.* 2020, 10, 8870–8879 Read Online

ACCESS | Metrics & More | Article Recommendations | Supporting Information

**ABSTRACT:** Copolymerization of $CO_2$ and cyclohexene oxide (CHO) upcycles $CO_2$ into the value-added, chemically recyclable, thermoplastic poly(cyclohexene carbonate) (PCHC). Using density functional theory, the Zn-catalyzed copolymerization mechanism has been characterized with a particular focus on the effects of chiral $\beta$-diiminate (BDI) ligands as they influence the reactivity and enantioselectivity in the epoxide ring-opening step, where the latter is required for isotacticity. Theory indicates that both mono- and binuclear forms of the catalyst are involved along the reaction path, with the turnover-limiting step being ring-opening of the epoxide mediated by a binuclear catalyst. Subsequent $CO_2$ insertion is predicted to be kinetically facile and preferentially mediated by a mononuclear catalyst. The predicted preference for epoxide opening to give *R,R*-stereocenters in the copolymer when *N*-(4-(((1*S*,2*S*)-2-(benzyloxy)cyclohexyl)amino)-5,5,5-trifluoropent-3-en-2-ylidene)-2,6-dimethylaniline is used as the BDI ligand agrees with the experiment and is attributed to differential ligand distortions associated with key non-bonded interactions in the competing transition-state structures. Further analysis predicts that 2,6-dichloro and dibromo substitutions of the BDI ligand *N*-aryl group(s) should result in increased rates and enantioselectivities for copolymerization.

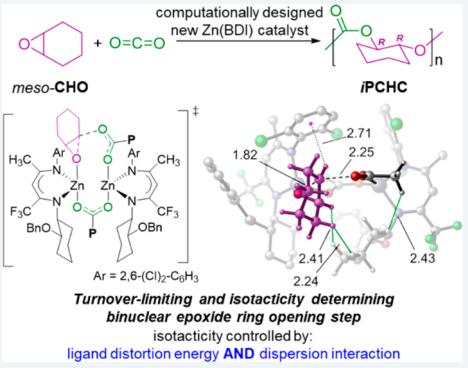


**KEYWORDS:** *catalysis, ligand effects, epoxide/$CO_2$ copolymerization, stereoselectivity, catalyst design, mechanistic investigation*



## INTRODUCTION

Cheap and effective polymer production is a key foundation of our convenient life nowadays, but traditional approaches pose environmental challenges.[1] Appealing sustainable alternatives include using renewable raw materials instead of fossil fuels, and especially so if the polymers produced are recyclable.[2] Within this category, alternating copolymerization of $CO_2$ and cyclohexene oxide (CHO) to produce thermoplastic poly(cyclohexene carbonate) (PCHC)[3] is particularly interesting because it upcycles $CO_2$ into value-added polymer products.[4] Despite the sustainability of the PCHC polymer, industrial applications of PCHC are limited because of its poor mechanical and thermal properties relative to traditional competitors.[5] However, studies have demonstrated that isotactic poly(cyclohexene carbonate) (*i*PCHC), which derives from enantioselection in the epoxide ring-opening step, has an elevated melting temperature ($T_m$).[6] In general, isotactic polymers are also expected to have better mechanical properties compared to their atactic analogues.[7] Moreover, *i*PCHCs are chemically recyclable, as thermal decomposition of *i*PCHC produces optically pure cyclic cyclohexene carbonate (cCHC). Purification and repolymerization of the cCHC regenerates virgin-quality *i*PCHC (Scheme 1).[8] Various homogeneous single-site catalysts have been reported, with a wide range of transition-metal centers and ligand systems, to

**Scheme 1. Zn(BDI)(OAc)-Catalyzed $CO_2$/CHO Copolymerization Reaction To Produce Chemically Recyclable *i*PCHC with High Enantioselectivity**

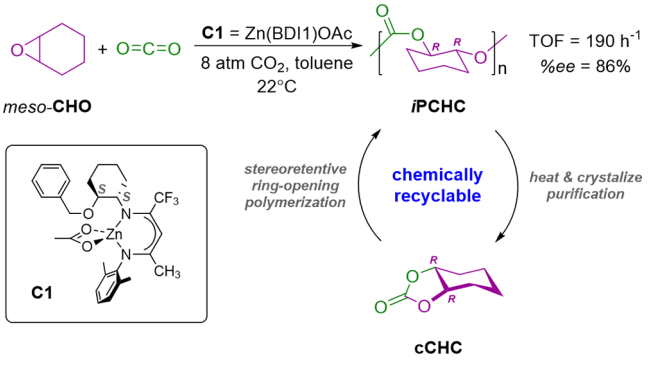


Received: May 24, 2020
Revised: July 14, 2020
Published: July 15, 2020




https://dx.doi.org/10.1021/acscatal.0c02299
*ACS Catal.* 2020, 10, 8870–8879

produce *i*PCHC from $CO_2$/CHO copolymerization with varying levels of turnover frequency (TOF), carbonate percentage, dispersity, and isotacticity control.[9−11] Among these, Zn-*β*-diiminate (BDI) catalysts are highly promising because they lead to essentially perfectly alternating polycarbonate from *meso*-CHO and $CO_2$ at low pressure. In 2014, Coates and co-workers reported a series of asymmetric BDI ligands that are effective for *i*PCHC production, and in particular catalyst **C1** was reported to copolymerize *meso*-CHO and $CO_2$ to produce *i*PCHC with >99% carbonate linkages, 86% ee (isotacticity), and a TOF of 190 $h^{-1}$ at room temperature and low $CO_2$ pressure in toluene (Scheme 1).[12]

Early mechanistic studies suggested that Zn(BDI)-catalyzed CHO/$CO_2$ copolymerization involves a binuclear catalyst.[13] A loosely bound binuclear complex derived from **C1** has been characterized by single-crystal X-ray crystallography.[12] A plausible reaction mechanism for Zn(BDI)-catalyzed CHO/$CO_2$ copolymerization is shown in Scheme 2, with the

**Scheme 2. Hypothesized Mechanism of Zn(BDI)-Catalyzed Copolymerization of $CO_2$ and Cyclohexene Oxide**

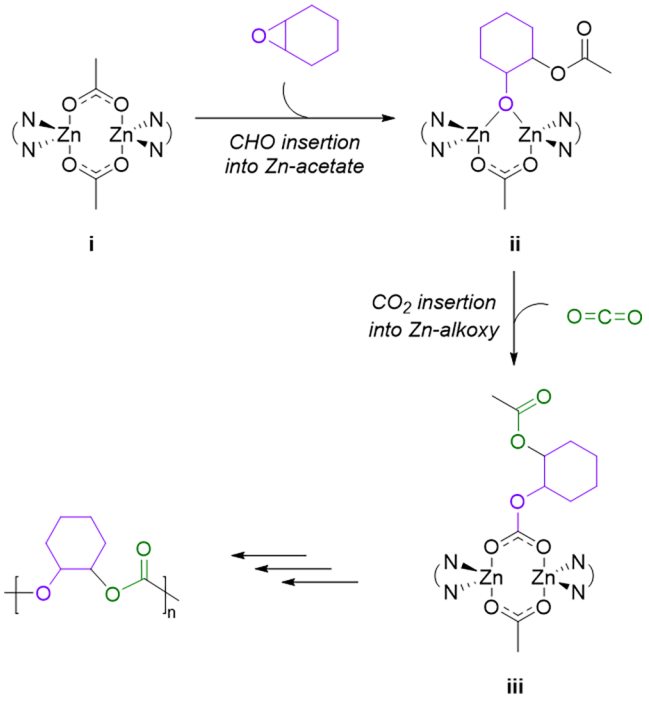


precatalyst likely to be the Zn-acetate dimer complex **i**. The insertion of CHO into the Zn-acetate bond forms the Zn-acetate/Zn-alkoxy binuclear complex **ii**. From intermediate **ii**, insertion of $CO_2$ into a Zn-alkoxy bond leads to the Zn-carbonate/Zn-acetate binuclear complex **iii**, which mimics the structure of the original Zn-acetate precatalyst and can continue the cycle, with possibly either one or two growing chains per binuclear complex.

Few computational studies have addressed the Zn(II)-catalyzed alternating copolymerization of epoxides and $CO_2$,[14] and none have considered the effects of asymmetric BDI ligands on enantioselectivity. Noting the flexibility of the dimeric Zn(BDI) catalyst, we surmise that noncovalent interactions are likely to be important in controlling enantioselectivity, and modern density functional theory (DFT) has proven useful for modeling such effects,[15] including in the context of computational catalysis. Here, we use such DFT calculations to characterize the reaction mechanism for the catalyzed $CO_2$/CHO copolymerization, to identify the basis of enantioselectivity, and finally to design a new generation of asymmetric *β*-diiminate Zn-catalysts predicted to provide both higher reactivity and enantioselectivity.[16]

## COMPUTATIONAL METHODS

All geometry optimizations were performed using the B3LYP-D3[17,18] functional with a mixed basis set of LANL2DZ[19] for Zn and 6-31G(d) for other atoms. Single-point energies were calculated with *ω*B97XD[20] and a mixed basis set of SDD[21] for Zn and 6-311+G(d,p) for other atoms. We have also studied the potential energy surface (PES) of the cycle of initiation at other levels of theory to assess sensitivity to choice of functional (see Supporting Information section 1 for details). Solvation effects were considered in the single-point energy calculations using the SMD[22] model in toluene ($\varepsilon$ = 2.37).[23] Reported Gibbs free energies and enthalpies include thermal contributions computed at 298 K and employ a standard-state concentration in solution of 1 M. All calculations were performed with the Gaussian 16 program.[24] Because the harmonic-oscillator approximation may lead to spurious results for the computed entropies in molecules with low-frequency vibrational modes, the quasi-harmonic approximation of Grimme was applied to compute the thermal corrections with a cutoff frequency of 50 $cm^{-1}$;[25] the *GoodVibes* package was used for this purpose.[26] Stand-alone dispersion energies were calculated using the DFTD3 program.[18]

## RESULTS AND DISCUSSION

Figure 1 presents the computed Gibbs free energy reaction coordinate at the $SMD_{(toluene)}$/*ω*B97XD/6-311+G(d,p),SDD-(Zn)//B3LYP-D3/6-31G(d),LANL2DZ(Zn) level of theory for the initiation step of the **C1**-catalyzed copolymerization of CHO and $CO_2$. For clarity, only the (*R*,*R*)-selective pathway, which leads to the experimentally observed product, is illustrated. Optimized geometries of key intermediates are provided in Figure 2. The basis of enantioselectivity will be discussed further later. The Gibbs free energies of all stationary points on the potential energy surface are reported with respect to the most stable Zn-acetate dimer complex **IM1** (see Supporting Information section 2 for discussion of the catalyst resting state). In the resting state of the initiation cycle, in which the Zn−Zn separation is relatively short (3.61 Å), the *N*-Ar groups and the *N*-cyclohexyl groups on the opposing BDI ligands are oriented to different sides, one to another, to minimize steric repulsion (Figure 2).

Coordination of the CHO substrate to form **IM2** is computed to be endergonic by 7.7 kcal/mol with respect to the preceding **IM1** (Figure 1). Because the Zn−Zn separation is elongated to 4.82 Å in **IM2**, the lowest-energy conformation accommodates the two *N*-Ar groups of the two BDI ligands on the same side as one another, which permits favorable C−H/*π* interactions with the CHO substrate (see Supporting Information section 3 for conformations of **IM2**). Subsequent CHO ring-opening by the Zn-coordinated acetate occurs with an activation free energy of 18.9 kcal/mol relative to **IM1**. The Zn-acetate/Zn-alkoxy binuclear complex **IM3** is 2.2 kcal/mol lower in free energy than **IM1**. Because of the asymmetric nature of the BDI ligand used, we systematically studied 16 conformations of **TS1** and **IM3** (see Supporting Information


https://dx.doi.org/10.1021/acscatal.0c02299
ACS Catal. 2020, 10, 8870−8879

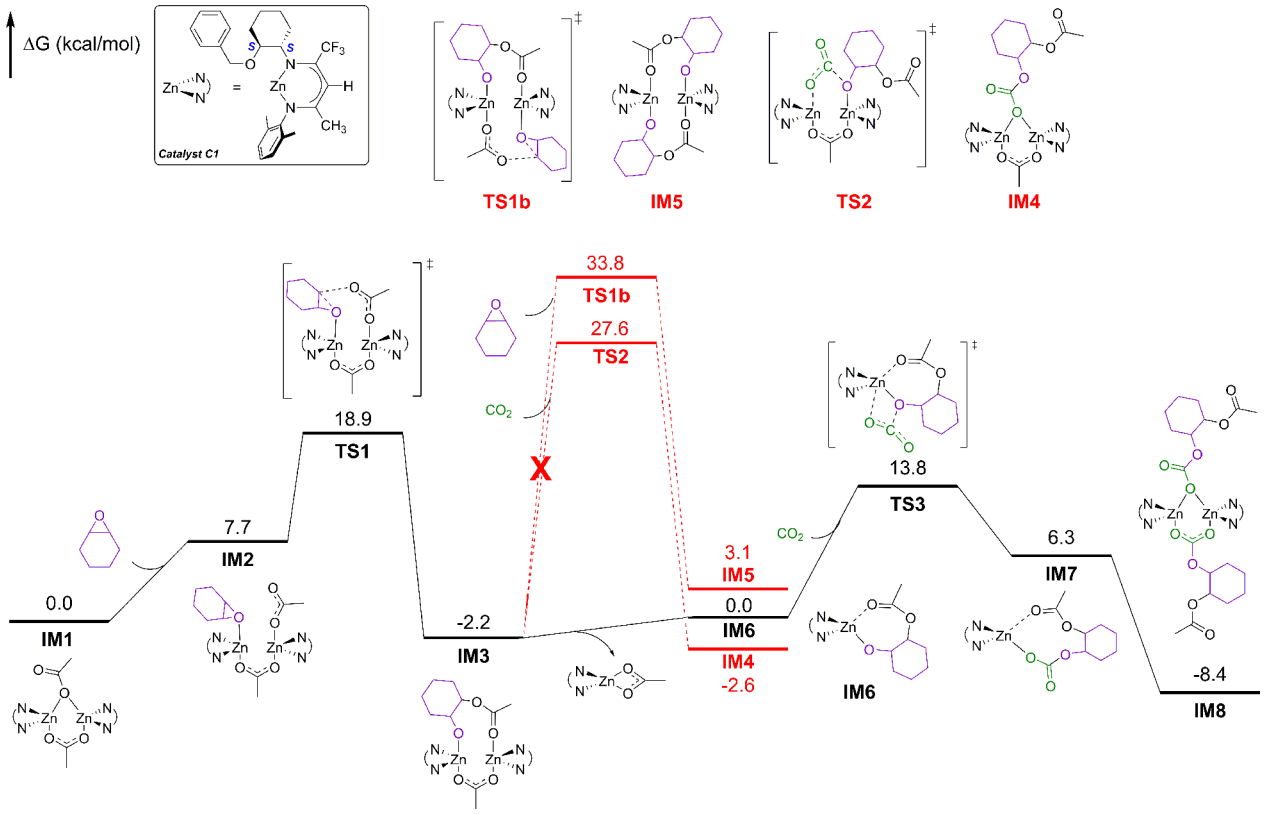


**Figure 1.** Computed potential energy surface for the initiation step of the Zn-catalyzed $CO_2$/CHO copolymerization reaction along the proposed dimer/monomeric mechanism.

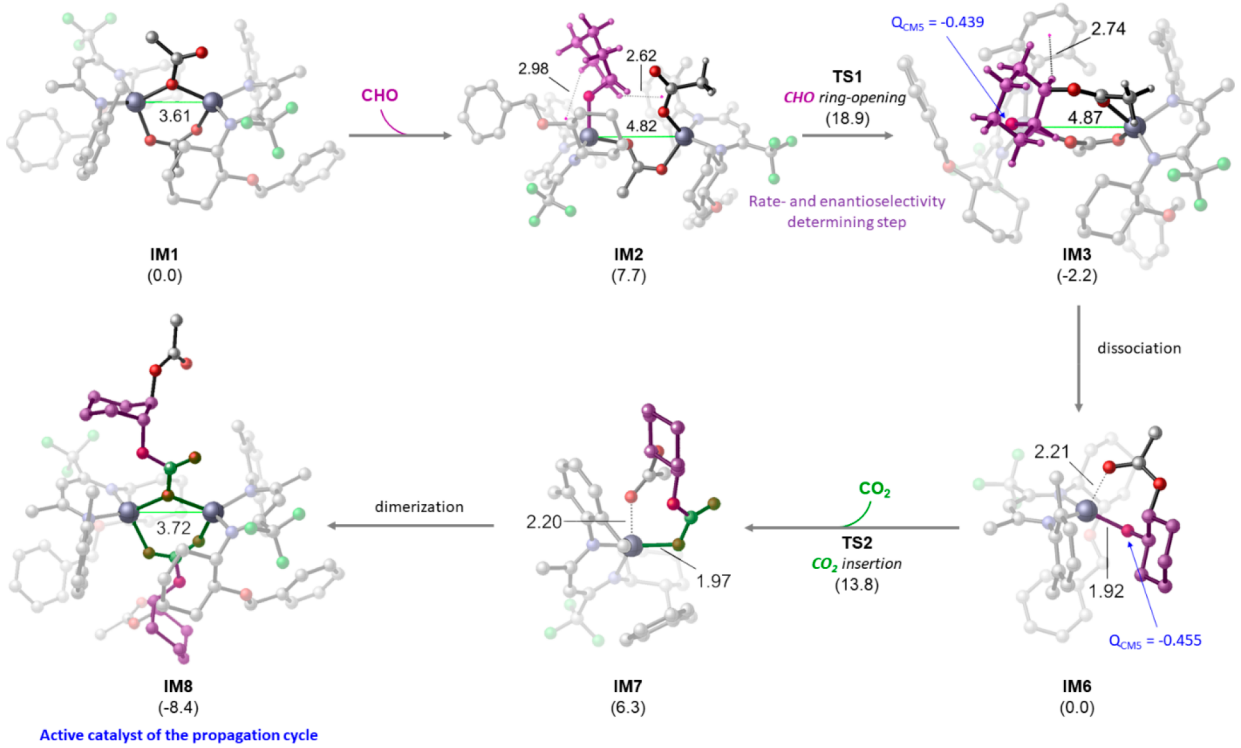


**Figure 2.** Selected geometric details for optimized intermediates along the mixed binuclear/mononuclear reaction path for initiation of CHO/$CO_2$ copolymerization (bond distances in Å; Gibbs free energies in kcal/mol relative to **IM1**).

section 4 for all other conformations). We have also considered a monomeric mechanism, along which CHO inserts into a Zn(BDI)(OAc) monomer. The monomeric ring-opening is computed to have a free energy of activation of 35.0 kcal/mol relative to a Zn(BDI)OAc monomer that is itself higher in energy than **IM1** (see Supporting Information



https://dx.doi.org/10.1021/acscatal.0c02299
ACS Catal. 2020, 10, 8870−8879

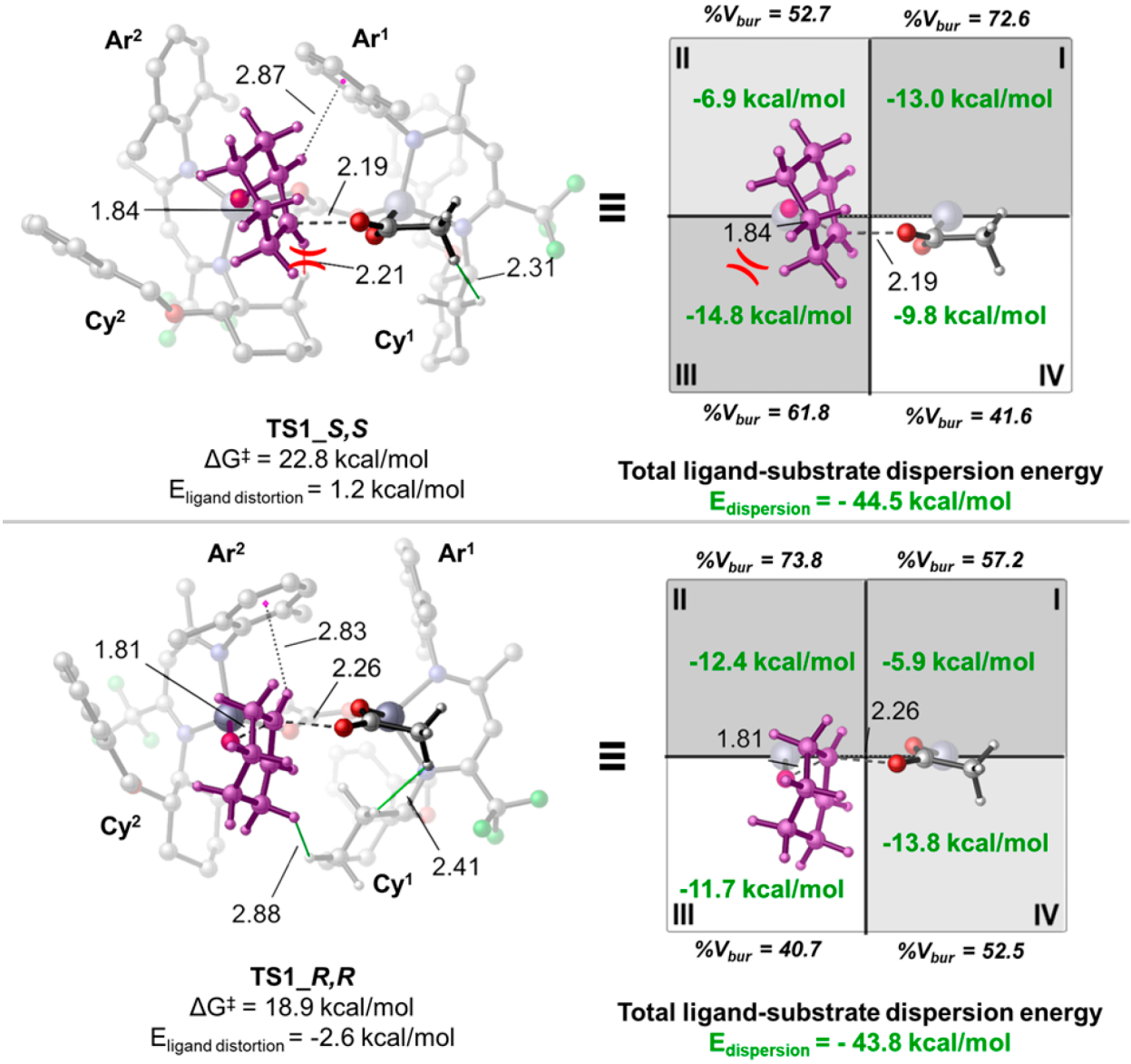


**Figure 3.** Optimized geometries determining enantioselection in CHO ring-opening transition states for the initiation of **C1**-catalyzed CHO/$CO_2$ copolymerization (selected bond distances are in Å).

section 5 for details), and we do not consider that process further. This prediction of preference for a bimetallic catalyst for this step is consistent with previous mechanistic studies by the Coates group.[12]

From **IM3**, we consider three alternative reactions (Figure 1). First, we consider $CO_2$ insertion into the bimetallic Zn-alkoxy (**TS2**),[27] which has a free energy of activation of 27.6 kcal/mol. Such a high activation energy is inconsistent with experimental rates at 0 °C, so we sought an alternative to this path. A second CHO insertion to generate another polymer chain through **TS1b** is predicted to have a still higher activation free energy (33.8 kcal/mol). As a third alternative, dissociation of the Zn-acetate/Zn-alkoxy binuclear complex **IM3** to form Zn-alkoxy monomer **IM6** (and Zn-acetate) is found to be thermal neutral with respect to **IM1** (0.0 kcal/mol), within the context of a 1 M standard state, which is considerably higher than the Zn concentration employed under experimental conditions. The Zn-alkoxy monomer **IM6** is stabilized by coordination of the backbone acetate group to the Zn center. The calculated CM5 charge[28] on the oxygen atom of the Zn-alkoxy bond suggests that the Zn-alkoxy group in **IM6** is only a very slightly better nucleophile ($Q_{CM5}$ = −0.455) than the Zn-alkoxy group in **IM3** ($Q_{CM5}$ = −0.439), but in any case $CO_2$ insertion through **TS3** (Figure 2) is predicted to have an activation free energy of only 13.8 kcal/mol (see Supporting Information sections 7 and 8 for higher-energy conformations of **IM6** and **TS3**, respectively) and leads to Zn-carbonate intermediate **IM7** at an energy 6.3 kcal/mol above **IM1**. Subsequent dimerization of **IM7** forms the Zn-carbonate dimer **IM8** and completes the cycle of initiation. Because **IM8** has a structure analogous to the precatalyst resting state **IM1**, it can be the initial intermediate employed for subsequent propagation cycles. Overall, then, the initiation of the Zn(BDI)-catalyzed $CO_2$/CHO copolymerization reaction takes place along a reaction path involving both mono- and binuclear catalysts, and the rate- and stereoselectivity determining step is the epoxide ring-opening step on the binuclear catalyst.


https://dx.doi.org/10.1021/acscatal.0c02299
ACS Catal. 2020, 10, 8870−8879

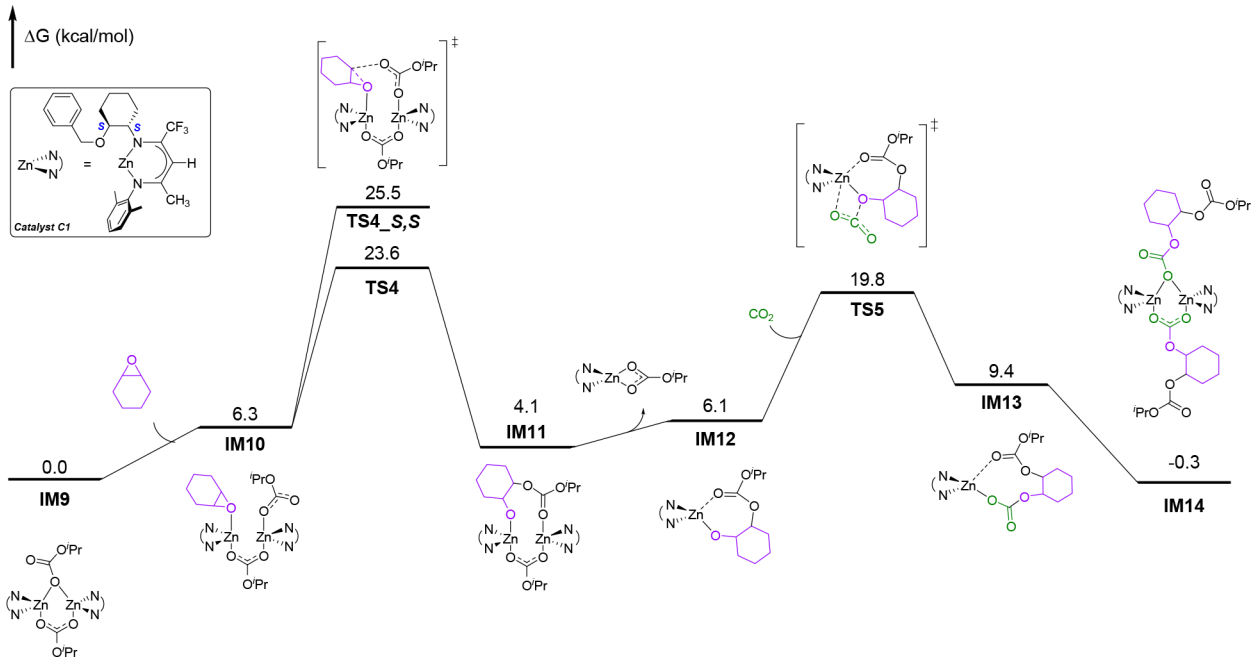


**Figure 4.** Computed potential energy surface of the 1st propagation cycle of the dimeric Zn-catalyzed $CO_2$/CHO copolymerization reaction.

We next focused on the binuclear CHO ring-opening transition-state (TS) structure **TS1** to explore the origin of its enantioselectivity. A thorough conformational search of possible CHO ring-opening TS structures found a total of 32 conformations (16 for each enantiomer), including both possible positionings of the *N*-aryl and *N*-cyclohexyl substitutions of the two BDI ligands relative to one another (see Supporting Information section 4 for details). For the lowest-energy conformations of **TS1_*R,R*** and **TS1_*S,S***, both the *N*-aryl substituents and the *N*-cyclohexyl groups of the two BDI ligands are oriented equivalently relative to one another (Figure 3). The calculated free energies of activation for **TS1_*R,R*** and **TS1_*S,S*** are 18.9 and 22.8 kcal/mol, respectively. The predicted *R,R*-stereoselectivity ($\Delta\Delta G^{\ddagger}$ = 3.9 kcal/mol) agrees well with the experiment.[12] Corresponding quadrant diagrams of **TS1_*R,R*** and **TS1_*S,S*** were generated to quantify the percentage buried volume ($\%V_{bur}$) associated with the steric environments created by each *N*-substituent, as well as to aid in understanding possible dispersion interactions between the BDI ligands and the substrates (CHO and both acetate groups) (Figure 3).[29] Supporting Information sections 9 and 10 detail the calculations of $\%V_{bur}$ and the ligand−substrate dispersion energies, respectively. In both quadrant diagrams, $Ar^1$ and $Ar^2$ locate in quadrants QI and QII, while $Cy^2$ and $Cy^1$ locate in quadrants QIII and QIV; we have partitioned calculated dispersion interaction energies between the CHO and acetate groups over the *N*-substituents in each quadrant.[18]

The calculated total ligand−substrate dispersion energies in **TS1_*R,R*** and **TS1_*S,S*** are −43.8 and −44.5 kcal/mol, respectively. Because of the small differences observed, we surmise that the ligand−substrate dispersion energy does little to differentiate **TS1_*R,R*** and **TS1_*S,S*** in the **C1**-catalyzed CHO/$CO_2$ copolymerization reaction. We also considered the effects of ligand distortion energy, arising in response to ligand−substrate steric interactions, on $\Delta\Delta G^{\ddagger}$ for **TS1_*R,R*** and **TS1_*S,S***. The calculated ligand distortion energies of **TS1_*R,R*** and **TS1_*S,S*** are −2.6 and 1.2 kcal/mol, correspondingly. The difference in ligand distortion energy favors **TS1_*R,R*** by 3.8 kcal/mol over **TS1_*S,S***, which suggests that this is the major factor contributing to **TS1_*R,R*** being lowest in energy.

Dispersion does play a significant role in affecting the geometries of the two TS structures, even if it does not lead to energetic differentiation between them. In **TS1_*R,R***, because of the stabilizing C−H/$\pi$ interaction with $Ar^2$ in QII, the *N*-$Ar^2$ tilts toward the CHO substrate and makes QII a sterically occupied quadrant ($\%V_{bur}$ = 73.8). Because both of the four-coordinated Zn(II) centers have near-tetrahedral geometries, if the *N*-$Ar^2$ group tilts toward the substrates, the $Cy^2$ group must tilt away, and this makes QIII a sterically less-occupied quadrant ($\%V_{bur}$ = 40.7). By contrast, in **TS1_*S,S***, because of the stabilizing C−H/$\pi$ interaction with $Ar^1$ in QI, the *N*-$Ar^1$ group tilts toward the CHO substrate and makes QI a sterically occupied quadrant ($\%V_{bur}$ = 72.6). To avoid steric repulsion between the two *N*-Ar groups, $Ar^2$ tilts away from the substrate, making QII in **TS1_*S,S*** a relatively less-occupied quadrant ($\%V_{bur}$ = 52.7), and the $Cy^2$ group tilts toward the substrates and makes QIII in **TS1_*S,S*** a sterically occupied quadrant ($\%V_{bur}$ = 61.8). These various interactions in **TS1_*R,R*** and **TS1_*S,S*** are predicted to stabilize both transition states equally when only dispersion energies are computed, but importantly, they lead ultimately to quite different steric environments. Thus, the sterically most demanding CHO group locates in the less-occupied QIII ($\%V_{bur}$ = 40.7) in **TS1_*R,R*** but locates instead in the more-occupied QIII ($\%V_{bur}$ = 61.8) in **TS1_*S,S***. This is the ligand distortion that favors **TS1_*R,R***.

Following this analysis of the initiation cycle, we next modeled propagation of the **C1**-catalyzed copolymerization of CHO and $CO_2$ at the SMD$_{(toluene)}$/$\omega$B97XD/6-311+G(d,p),SDD(Zn)//B3LYP-D3/6-31G(d),LANL2DZ(Zn) level of theory with an O$^i$Pr substituent to model the growing carbonate-terminated polymer. Gibbs free energies for all stationary points on the potential energy surface are reported


https://dx.doi.org/10.1021/acscatal.0c02299
ACS Catal. 2020, 10, 8870−8879

**Table 1. Effects of Different *N*-Ar Substitutions on the Rate and Enantioselectivity of the Initiation Cycle of the CHO/$CO_2$ Copolymerization Reaction (Free Energies in kcal/mol)**

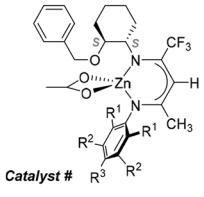


| catalyst | $R^1$ = | $R^2$ = | $R^3$ = | $\Delta G^{\ddagger}_{R,R}$ | $\Delta G^{\ddagger}_{S,S}$ | $\Delta\Delta G^{\ddagger}$ |
|---|---|---|---|---|---|---|
| **C1** | Me | H | H | 18.9 | 22.8 | 3.9 |
| **C2** | H | Me | H | 21.4 | 20.9 | -0.5 |
| **C3** | H | H | H | 21.6 | 21.4 | -0.2 |
| **C4** | $CF_3$ | H | H | 21.0 | 24.8 | 3.8 |
| **C5** | Et | H | H | 19.5 | 24.8 | 5.3 |
| **C6** | *i*Pr | H | H | 24.0 | 29.9 | 5.9 |
| **C7** | F | H | H | 16.7 | 19.3 | 2.7 |
| **C8** | F | H | F | 16.2 | 19.1 | 3.0 |
| **C9** | F | F | F | 17.8 | 19.4 | 1.5 |
| **C10** | Cl | H | H | 17.0 | 22.4 | 5.4 |
| **C11** | Br | H | H | 17.8 | 23.4 | 5.6 |

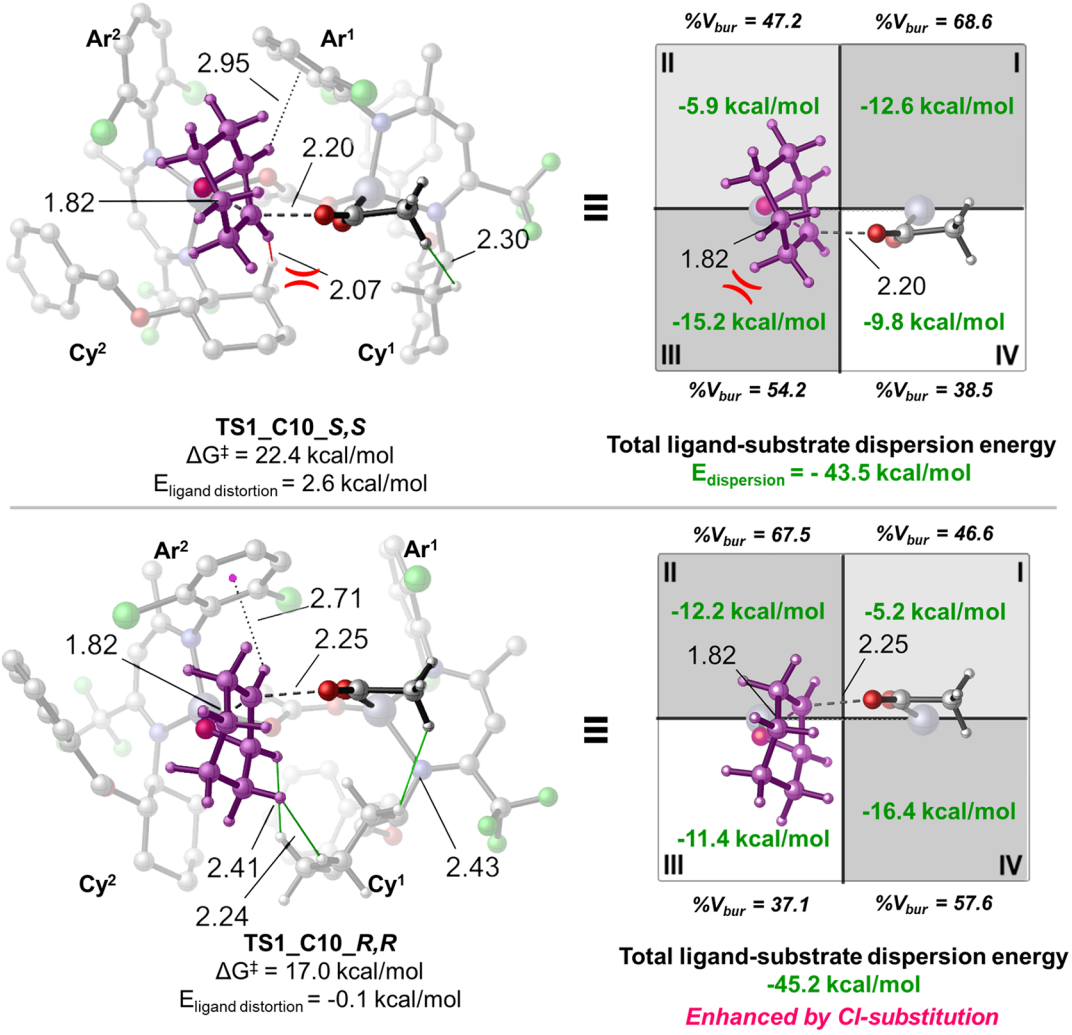


**Figure 5.** Optimized geometries determining enantioselection in CHO ring-opening transition states for the initiation of **C10**-catalyzed CHO/$CO_2$ copolymerization (selected bond distances are in Å).

with respect to the initial Zn-carbonate dimer complex **IM9** (Figure 4).

Propagation proceeds via a mixed binuclear/mononuclear reaction mechanism analogous to that for initiation (Figure 1).



https://dx.doi.org/10.1021/acscatal.0c02299
ACS Catal. 2020, 10, 8870−8879

The dimeric epoxide ring-opening step (**TS4**) to generate *R,R* stereochemistry has a free energy of activation of 23.6 kcal/mol. The subsequent mononuclear $CO_2$ insertion (**TS5**) has a lower free energy of activation relative to **IM9**, 19.8 kcal/mol (for the 1 M standard state; it will be lower for smaller concentrations of total Zn). Thus, **TS4** is the rate- and stereodetermining step for propagation (see Supporting Information section 11 for less-favorable pathways). The calculated difference in free energy of activation between **TS4_*R,R*** and **TS4_*S,S*** is 1.9 kcal/mol, consistent with the *R,R* enantioselectivity in the polymer reported by the Coates group.[12] The addition of 2 CHO monomers (one to each growing chain) is slightly exergonic by 0.3 kcal/mol at the chosen level of theory. Predictions of overall polymerization free energies do tend to underestimate experimental values, in part owing to quantum chemical calculations failing to sample the full conformational phase space available to growing polymer chains and thus underestimating their entropies. There may also be favorable nonbonded interactions that stabilize secondary structure in growing polymer chains, and these cannot be captured when modeling only the first propagation step.

Having assessed those factors responsible for enantioselectivity in the copolymerization, we next assessed how the choice of substituents on the BDI ligand might affect reactivity and stereoselection. We considered modification of the BDI ligand on both the *N*-aryl group (**C2**−**C11**) and the ligand backbone substitutions (**C12**−**C17**, in Supporting Information section 12). Noting that the binuclear-catalyzed CHO ring-opening step is the rate- and stereoselectivity determining step, we computed differential free energies of activation for **TS1_*R,R*** vs **TS1_*S,S*** for all of the **C2**−**C17** catalysts. The BDI *N*-aryl substitutions (**C2**−**C11**, Table 1) are computed to influence calculated free energies of activation for **TS1_*R,R*** and **TS1_*S,S*** much more significantly than substitution of the BDI ligand backbone (**C12**−**C17**), so our remaining discussion will focus only on the former (see Supporting Information section 12 for details on the latter).

Compared to **C1** (2,6-$(CH_3)_2$-$C_6H_3$), the calculated $\Delta\Delta G^{\ddagger}$ values for catalysts **C2** (3,5-$(CH_3)_2$-$C_6H_3$) and **C3** ($C_6H_5$) are very small in magnitude, i.e., their enantioselectivity is predicted to be minimal. Considering the set of fluoro-substituted catalysts **C7**, **C8**, and **C9**, both 2,6-difluoro-substitution of the *N*-aryl group (**C7**) and 2,4,6-trifluoro-substitution (**C8**) are predicted to accelerate the rate of ring-opening. Interestingly, for perfluoro-substituted **C9**, the acceleration relative to **C1** is computed to be slightly smaller than those with **C7** and **C8**. Moreover, the enantioselectivity is predicted to be lower than those for **C1**, **C7**, and **C8**. Noting that the electronic effect of 4-substitution of the *N*-aryl group (para) is expected to be no different than 2- or 6-substitution (ortho), and noting the substantially greater propensity for 2,6-substitution to influence the aryl ring rotations and steric interactions with substrates, we focused further analysis on variations in reactivity as a function of 2,6-substitution. Considering **C4** (2,6-$(CF_3)_2$-$C_6H_3$), trifluoromethyl-substitution slows reactivity relative to **C1** and slightly reduces selectivity. Considering aliphatic groups larger than methyl (**C5** and **C6**), bulkier ortho-substituents increase the predicted enantioselectivity, but they do so at the cost of the predicted rate, with **C5** and **C6** having free energies of activation through **TS1_*R,R*** greater than those for **C1** by 0.6 and 5.1 kcal/mol, respectively. This prediction is consistent with our analysis earlier that bulkier *N*-Ar groups should promote enantioselectivity by greater steric destabilization of **TS1_*S,S***. With hopes of maintaining lower overall free energies of activation, we next considered 2,6-dichloro- and 2,6-dibromo-substitutions (**C10** and **C11**), and in both instances, calculations predict lower $\Delta G^{\ddagger}$ values and higher $\Delta\Delta G^{\ddagger}$ values, i.e., we predict these catalysts to be both faster and more enantioselective relative to **C1**.

Noting the optimal performance computed for **C10**, we explored the details of **TS1_C10_*R,R*** and **TS1_C10_*S,S*** to better understand the origin of the high predicted enantioselectivity (Figure 5; the complete potential energy surface for initiation with **C10** is in Supporting Information section 13). The favorable ligand−substrate dispersion energy is greater in **TS1_C10_*R,R*** (−45.2 kcal/mol) than in **TS1_C10_*S,S*** (−43.5 kcal/mol). This derives primarily from the van der Waals interaction between the CHO substrate and the $Cy^1$ group in QIV (−16.4 kcal/mol), with QIV of **TS1_C10_*R,R*** being sterically more occupied (%$V_{bur}$ = 52.5) than QIV of **TS1_C10_*S,S*** (%$V_{bur}$ = 38.5); key H−H distances between CHO and $Cy^1$ in **TS1_C10_*R,R*** are 2.24 and 2.41 Å. In addition, as described earlier for the case for **C1**, in **TS1_C10_*R,R*** the sterically demanding CHO substrate locates in the sterically less-occupied QIII (%$V_{bur}$ = 37.1), which leads to a small ligand distortion energy (0.0 kcal/mol). In **TS1_C10_*S,S***, by contrast, the CHO substrate locates in the sterically more occupied QIII (%$V_{bur}$ = 54.2), which leads to a larger ligand distortion energy (2.6 kcal/mol). The combination of these two effects, both of which stabilize **TS1_C10_*R,R*** relative to **TS1_C10_*S,S***, contribute to the large predicted enantioselectivity ($\Delta\Delta G^{\ddagger}$ = 5.4 kcal/mol, >99% ee).[30]

While the analysis just presented focuses on the initiation step, we also computed the influence of 2,6-dichloro-substitution of the *N*-aryl group on the full propagation cycle. The predicted free energies of activation associated with **TS4_C10_*R,R*** and **TS4_C10_*S,S*** are 20.6 and 24.1 kcal/mol, respectively. The predicted $\Delta\Delta G^{\ddagger}$ of 3.5 kcal/mol is smaller than the 5.4 kcal/mol predicted for initiation but still larger than the corresponding propagation value predicted for **C1** (1.9 kcal/mol; vide supra). Thus, catalyst **C10** is a promising candidate as a next-generation catalyst for CHO/$CO_2$ copolymerization.

## CONCLUSION

Computed reaction coordinates indicate that CHO/$CO_2$ copolymerization catalyzed by Zn(BDI) proceeds via a mechanism that involves both dimeric and monomeric catalysts. Ring-opening of CHO by acetate (initiation) or carbonate (propagation) is catalyzed by dimeric Zn(BDI), while $CO_2$ insertion into a Zn-alkoxy preferentially occurs for Zn(BDI) monomer. The CHO ring-opening step is predicted both to be turnover-limiting and to determine enantioselection (which equates to polymer isotacticity). The computed enantioselectivity, which has a magnitude consistent with the experiment for known catalyst **C1**, is found to be associated with differential ligand distortion energies imparted through accommodation of substrates in competing transition-state structures. When methyl substituents at the 2- and 6-positions of the *N*-aryl groups of the BDI ligand, as found in **C1**, are replaced with chloro and bromo atoms, theory predicts that both the rate and the enantioselection for CHO/$CO_2$ copolymerization should increase, with chloro being the


https://dx.doi.org/10.1021/acscatal.0c02299
ACS Catal. 2020, 10, 8870−8879

optimum choice. The rate acceleration and increased enantioselectivity are found to derive from improved dispersion interactions that further stabilize the turnover-limiting transition-state structures relative to **C1** and further discriminate between structures, leading to *R,R* vs *S,S* ring-opened products. These results suggest that the use of halogen-substituted catalysts should be tested and further provide a rational basis for ongoing catalyst improvement.

## ■ ASSOCIATED CONTENT

### Supporting Information

The Supporting Information is available free of charge at https://pubs.acs.org/doi/10.1021/acscatal.0c02299.

Additional computational results (PDF)

Cartesian coordinates (PDF)

## ■ AUTHOR INFORMATION


### Corresponding Author

**Huiling Shao** − *Department of Chemistry, Minnesota Supercomputing Institute, and Chemical Theory Center, University of Minnesota, Minneapolis, Minnesota 55455, United States;* orcid.org/0000-0001-8007-6408; Email: shaoh@umn.edu

### Authors

**Yernaidu Reddi** − *Department of Chemistry, Minnesota Supercomputing Institute, and Chemical Theory Center, University of Minnesota, Minneapolis, Minnesota 55455, United States;* orcid.org/0000-0002-6743-9582

**Christopher J. Cramer** − *Department of Chemistry, Minnesota Supercomputing Institute, and Chemical Theory Center, University of Minnesota, Minneapolis, Minnesota 55455, United States;* orcid.org/0000-0001-5048-1859

Complete contact information is available at: https://pubs.acs.org/10.1021/acscatal.0c02299


### Notes

The authors declare no competing financial interest.

## ■ ACKNOWLEDGMENTS

Funding for this project was provided by the Center for Sustainable Polymers, a National Science Foundation supported Center for Chemical Innovation (CHE-1901635). We thank the Minnesota Supercomputing Institute (MSI) for providing key computational resources

## ■ REFERENCES


(1) (a) Stevens, E. S. *Green plastics: an introduction to the new science of biodegradable plastics*; Princeton University Press: 2002. (b) van der Ploeg, F. Natural resources: curse or blessing? *J. Econ. Lit.* **2011**, *49*, 366−420.

(2) (a) Zhu, Y.; Romain, C.; Williams, C. K. Sustainable polymers from renewable resources. *Nature* **2016**, *540*, 354−362. (b) Rieger, B., Künkel, A., Coates, G. W., Reichardt, R., Dinjus, E., Zevaco, T. A., Eds. *Synthetic biodegradable polymers*; Springer Science & Business Media: 2012; Vol. 245. (c) Schneiderman, D. K.; Hillmyer, M. A. 50th anniversary perspective: There is a great future in sustainable polymers. *Macromolecules* **2017**, *50*, 3733−3749.

(3) Reviews of $CO_2$/CHO copolymerization: (a) Inoue, S.; Koinuma, H.; Tsuruta, T. Copolymerization of carbon dioxide and epoxide. *J. Polym. Sci., Part B: Polym. Lett.* **1969**, *7*, 287−292. (b) Inoue, S.; Koinuma, H.; Tsuruta, T. Copolymerization of carbon dioxide and epoxide with organometallic compounds. *Makromol. Chem.* **1969**, *130*, 210−220. (c) Klaus, S.; Lehenmeier, M. W.; Anderson, C. E.; Rieger, B. Recent advances in $CO_2$/epoxide copolymerization—New strategies and cooperative mechanisms. *Coord. Chem. Rev.* **2011**, *255*, 1460−1479. (d) Kozak, C. M.; Ambrose, K.; Anderson, T. S. Copolymerization of carbon dioxide and epoxides by metal coordination complexes. *Coord. Chem. Rev.* **2018**, *376*, 565−587. (e) Darensbourg, D. J.; Wilson, S. J. What's new with $CO_2$? Recent advances in its copolymerization with oxiranes. *Green Chem.* **2012**, *14*, 2665−2671. (f) Darensbourg, D. J.; Yeung, A. D. A concise review of computational studies of the carbon dioxide−epoxide copolymerization reactions. *Polym. Chem.* **2014**, *5*, 3949−3962.

(4) (a) Sakakura, T.; Choi, J. C.; Yasuda, H. Transformation of carbon dioxide. *Chem. Rev.* **2007**, *107*, 2365−2387. (b) Lee, S. H.; Cyriac, A.; Jeon, J. Y.; Lee, B. Y. Preparation of thermoplastic polyurethanes using in situ generated poly(propylene carbonate)-diols. *Polym. Chem.* **2012**, *3*, 1215−1220. (c) von der Assen, N.; Voll, P.; Peters, M.; Bardow, A. Life cycle assessment of $CO_2$ capture and utilization: a tutorial review. *Chem. Soc. Rev.* **2014**, *43*, 7982−7994. (d) Markewitz, P.; Kuckshinrichs, W.; Leitner, W.; Linssen, J.; Zapp, P.; Bongartz, R.; Schreiber, A.; Müller, T. E. Worldwide innovations in the development of carbon capture technologies and the utilization of $CO_2$. *Energy Environ. Sci.* **2012**, *5*, 7281−7305. (e) Chapman, A. M.; Keyworth, C.; Kember, M. R.; Lennox, A. J. J.; Williams, C. K. Adding value to power station captured CO2: tolerant Zn and Mg homogeneous catalysts for polycarbonate polyol production. *ACS Catal.* **2015**, *5*, 1581−1588.

(5) Luinstra, G. A. Poly (propylene carbonate), old copolymers of propylene oxide and carbon dioxide with new interests: catalysis and material properties. *Polym. Rev.* **2008**, *48*, 192−219.

(6) Wu, G. P.; Jiang, S. D.; Lu, X. B.; Ren, W. M.; Yan, S. K. Stereoregular poly (cyclohexene carbonates): Unique crystallization behavior. *Chin. J. Polym. Sci.* **2012**, *30*, 487−492.

(7) (a) Worch, J. C.; Prydderch, H.; Jimaja, S.; Bexis, P.; Becker, M. L.; Dove, A. P. Stereochemical enhancement of polymer properties. *Nat. Rev. Chem.* **2019**, *3*, 514−535. (b) Wang, Y.; Darensbourg, D. J. Carbon dioxide-based functional polycarbonates: Metal catalyzed copolymerization of CO2 and epoxides. *Coord. Chem. Rev.* **2018**, *372*, 85−100. (c) Gómez, F. J.; Waymouth, R. M. Catalysts rise to the challenge. *Science* **2002**, *295*, 635−636.

(8) (a) Hong, M.; Chen, E. Y. X. Chemically recyclable polymers: a circular economy approach to sustainability. *Green Chem.* **2017**, *19*, 3692−3706. (b) Liu, Y.; Zhou, H.; Guo, J. Z.; Ren, W. M.; Lu, X. B. Completely recyclable monomers and polycarbonate: approach to sustainable polymers. *Angew. Chem., Int. Ed.* **2017**, *56*, 4862−4866. (c) Guerin, W.; Diallo, A. K.; Kirilov, E.; Helou, M.; Slawinski, M.; Brusson, J. M.; Carpentier, J. F.; Guillaume, S. M. Enantiopure isotactic PCHC synthesized by ring-opening polymerization of cyclohexene carbonate. *Macromolecules* **2014**, *47*, 4230−4235.

(9) D'Auria, I.; D'Alterio, M. C.; Talarico, G.; Pellecchia, C. Alternating Copolymerization of CO2 and Cyclohexene Oxide by New Pyridylamidozinc (II) Catalysts. *Macromolecules* **2018**, *51*, 9871−9877.

(10) Isotactic copolymerization of $CO_2$ and CHO with transition metal-based catalysts other than zinc: (a) Cohen, C. T.; Thomas, C. M.; Peretti, K. L.; Lobkovsky, E. B.; Coates, G. W. Copolymerization of cyclohexene oxide and carbon dioxide using (salen) Co (III) complexes: synthesis and characterization of syndiotactic poly (cyclohexene carbonate). *Dalton Trans.* **2006**, *1*, 237−249. (b) Shi, L.; Lu, X. B.; Zhang, R.; Peng, X. J.; Zhang, C. Q.; Li, J. F.; Peng, X. M. Asymmetric alternating copolymerization and terpolymerization of epoxides with carbon dioxide at mild conditions. *Macromolecules* **2006**, *39*, 5679−5685. (c) Nishioka, K.; Goto, H.; Sugimoto, H. Dual catalyst system for asymmetric alternating copolymerization of carbon dioxide and cyclohexene oxide with chiral aluminum complexes: Lewis base as catalyst activator and Lewis acid as monomer activator. *Macromolecules* **2012**, *45*, 8172−8192. (d) Li, B.; Zhang, R.; Lu, X. B. Stereochemistry control of the alternating copolymerization of CO2 and propylene oxide catalyzed by SalenCrX complexes. *Macro-*

*molecules* **2007**, *40*, 2303−2307. (e) Nakano, K.; Nakamura, M.; Nozaki, K. Alternating copolymerization of cyclohexene oxide with carbon dioxide catalyzed by (salalen) CrCl complexes. *Macromolecules* **2009**, *42*, 6972−6980. (f) Liu, Y.; Fang, L. M.; Ren, B. H.; Lu, X. B. Asymmetric Alternating Copolymerization of CO2 with meso-Epoxides: Ring Size Effects of Epoxides on Reactivity, Enantioselectivity, Crystallization, and Degradation. *Macromolecules* **2020**, *53*, 2912−2918.

(11) Isotactic copolymerization of $CO_2$ and CHO with Zn-catalysts: (a) Cheng, M.; Lobkovsky, E. B.; Coates, G. W. Catalytic Reactions Involving C1 Feedstocks: New High-Activity Zn(II)-Based Catalysts for the Alternating Copolymerization of Carbon Dioxide and Epoxides. *J. Am. Chem. Soc.* **1998**, *120*, 11018−11019. (b) Nozaki, K.; Nakano, K.; Hiyama, T. Optically active polycarbonates: asymmetric alternating copolymerization of cyclohexene oxide and carbon dioxide. *J. Am. Chem. Soc.* **1999**, *121*, 11008−11009. (c) Nakano, K.; Nozaki, K.; Hiyama, T. Spectral Assignment of Poly [cyclohexene oxide-alt-carbon dioxide]. *Macromolecules* **2001**, *34*, 6325−6332. (d) Cheng, M.; Darling, N. A.; Lobkovsky, E. B.; Coates, G. W. Enantiomerically-enriched organic reagents via polymer synthesis: enantioselective copolymerization of cycloalkene oxides and CO2 using homogeneous, zinc-based catalysts. *Chem. Commun.* **2000**, *20*, 2007−2008. (e) Xiao, Y.; Wang, Z.; Ding, K. Copolymerization of cyclohexene oxide with CO2 by using intramolecular dinuclear zinc catalysts. *Chem. - Eur. J.* **2005**, *11*, 3668−3678. (f) Nakano, K.; Nozaki, K.; Hiyama, T. Asymmetric alternating copolymerization of cyclohexene oxide and CO2 with dimeric zinc complexes. *J. Am. Chem. Soc.* **2003**, *125*, 5501−5510. (g) Cheng, M.; Moore, D. R.; Reczek, J. J.; Chamberlain, B. M.; Lobkovsky, E. B.; Coates, G. W. Single-Site $\beta$-Diiminate Zinc Catalysts for the Alternating Copolymerization of CO2 and Epoxides: Catalyst Synthesis and Unprecedented Polymerization Activity. *J. Am. Chem. Soc.* **2001**, *123*, 8738−8749. (h) Moore, D. R.; Cheng, M.; Lobkovsky, E. B.; Coates, G. W. Electronic and Steric Effects on Catalysts for CO2/Epoxide Polymerization: Subtle Modifications Resulting in Superior Activities. *Angew. Chem., Int. Ed.* **2002**, *41*, 2599−2602. (i) Kim, J. G.; Cowman, C. D.; LaPointe, A. M.; Wiesner, U.; Coates, G. W. Tailored Living Block Copolymerization: Multiblock Poly(cyclohexene carbonates with Sequence Control. *Macromolecules* **2011**, *44*, 1110−1113.

(12) Ellis, W. C.; Jung, Y.; Mulzer, M.; Di Girolamo, R.; Lobkovsky, E. B.; Coates, G. W. Copolymerization of CO2 and meso epoxides using enantioselective $\beta$-diiminate catalysts: a route to highly isotactic polycarbonates. *Chem. Sci.* **2014**, *5*, 4004−4011.

(13) (a) Shi, L.; Lu, X. B.; Zhang, R.; Peng, X. J.; Zhang, C. Q.; Li, J. F.; Peng, X. M. Asymmetric alternating copolymerization and terpolymerization of epoxides with carbon dioxide at mild conditions. *Macromolecules* **2006**, *39*, 5679−5685. (b) Moore, D. R.; Cheng, M.; Lobkovsky, E. B.; Coates, G. W. Mechanism of the alternating copolymerization of epoxides and CO2 using $\beta$-diiminate zinc catalysts: evidence for a bimetallic epoxide enchainment. *J. Am. Chem. Soc.* **2003**, *125*, 11911−11924.

(14) (a) Liu, Z.; Torrent, M.; Morokuma, K. Molecular orbital study of zinc (II)-catalyzed alternating copolymerization of carbon dioxide with epoxide. *Organometallics* **2002**, *21*, 1056−1071. (b) Lehenmeier, M. W.; Bruckmeier, C.; Klaus, S.; Dengler, J. E.; Deglmann, P.; Ott, A. K.; Rieger, B. Differences in Reactivity of Epoxides in the Copolymerisation with Carbon Dioxide by Zinc-Based Catalysts: Propylene Oxide versus Cyclohexene Oxide. *Chem. - Eur. J.* **2011**, *17*, 8858−8869. (c) Buchard, A.; Jutz, F.; Kember, M. R.; White, A. J.; Rzepa, H. S.; Williams, C. K. Experimental and computational investigation of the mechanism of carbon dioxide/cyclohexene oxide copolymerization using a dizinc catalyst. *Macromolecules* **2012**, *45*, 6781−6795.

(15) (a) Yang, Y.; Perry, I. B.; Lu, G.; Liu, P.; Buchwald, S. L. Copper-catalyzed asymmetric addition of olefin-derived nucleophiles to ketones. *Science* **2016**, *353*, 144−150. (b) Wheeler, S. E.; Seguin, T. J.; Guan, Y.; Doney, A. C. Noncovalent interactions in organocatalysis and the prospect of computational catalyst design. *Acc. Chem. Res.* **2016**, *49*, 1061−1069. (c) Reddi, Y.; Tsai, C. C.; Avila, C. M.; Toste, F. D.; Sunoj, R. B. Harnessing Noncovalent Interactions in Dual-Catalytic Enantioselective Heck−Matsuda Arylation. *J. Am. Chem. Soc.* **2019**, *141*, 998−1009.

(16) (a) Poree, C.; Schoenebeck, F. A holy grail in chemistry: Computational catalyst design: Feasible or fiction? *Acc. Chem. Res.* **2017**, *50*, 605−608. (b) Thomas, A. A.; Speck, K.; Kevlishvili, I.; Lu, Z.; Liu, P.; Buchwald, S. L. Mechanistically Guided Design of Ligands That Significantly Improve the Efficiency of CuH-Catalyzed Hydroamination Reactions. *J. Am. Chem. Soc.* **2018**, *140*, 13976−13984.

(17) (a) Lee, C.; Yang, W.; Parr, R. G. Development of the Colle-Salvetti correlation-energy formula into a functional of the electron density. *Phys. Rev. B: Condens. Matter Mater. Phys.* **1988**, *37*, 785. (b) Becke, A. D. Density-functional exchange-energy approxima-tion with correct asymptotic behavior. *Phys. Rev. A: At., Mol., Opt. Phys.* **1988**, *38*, 3098. (c) Miehlich, B.; Savin, A.; Stoll, H.; Preuss, H. Results obtained with the correlation energy density functionals of Becke and Lee, Yang and Parr. *Chem. Phys. Lett.* **1989**, *157*, 200−206. (d) Becke, A. D. Density-functional thermochemistry. III. The role of exact exchange. *J. Chem. Phys.* **1993**, *98*, 5648−5652.

(18) Grimme, S. Semiempirical GGA-type density functional constructed with a long-range dispersion correction. *J. Comput. Chem.* **2006**, *27*, 1787−1799.

(19) Roy, L. E.; Hay, P. J.; Martin, R. L. Revised basis sets for the LANL effective core potentials. *J. Chem. Theory Comput.* **2008**, *4*, 1029−1031.

(20) Chai, J. D.; Head-Gordon, M. Long-range corrected hybrid density functionals with damped atom−atom dispersion corrections. *Phys. Chem. Chem. Phys.* **2008**, *10*, 6615−6620.

(21) Weigend, F.; Ahlrichs, R. Balanced basis sets of split valence, triple zeta valence and quadruple zeta valence quality for H to Rn: Design and assessment of accuracy. *Phys. Chem. Chem. Phys.* **2005**, *7*, 3297−3305.

(22) Marenich, A. V.; Cramer, C. J.; Truhlar, D. G. Universal solvation model based on solute electron density and on a continuum model of the solvent defined by the bulk dielectric constant and atomic surface tensions. *J. Phys. Chem. B* **2009**, *113*, 6378−6396.

(23) Weaver, J. H.; Frederikse, H. P. R. *CRC Handbook of Chemistry and Physics*; CRC Press: Boca Raton, FL, 1977; Vol. *76*, pp 12−156.

(24) Frisch, M. J.; Trucks, G. W.; Schlegel, H. B.; Scuseria, G. E.; Robb, M. A.; Cheeseman, J. R.; Scalmani, G.; Barone, V.; Petersson, G. A.; Nakatsuji, H.; Li, X.; Caricato, M.; Marenich, A. V.; Bloino, J.; Janesko, B. G.; Gomperts, R.; Mennucci, B.; Hratchian, H. P.; Ortiz, J. V.; Izmaylov, A. F.; Sonnenberg, J. L.; Williams-Young, D.; Ding, F.; Lipparini, F.; Egidi, F.; Goings, J.; Peng, B.; Petrone, A.; Henderson, T.; Ranasinghe, D.; Zakrzewski, V. G.; Gao, J.; Rega, N.; Zheng, G.; Liang, W.; Hada, M.; Ehara, M.; Toyota, K.; Fukuda, R.; Hasegawa, J.; Ishida, M.; Nakajima, T.; Honda, Y.; Kitao, O.; Nakai, H.; Vreven, T.; Throssell, K.; Montgomery, J. A., Jr.; Peralta, J. E.; Ogliaro, F.; Bearpark, M. J.; Heyd, J. J.; Brothers, E. N.; Kudin, K. N.; Staroverov, V. N.; Keith, T. A.; Kobayashi, R.; Normand, J.; Raghavachari, K.; Rendell, A. P.; Burant, J. C.; Iyengar, S. S.; Tomasi, J.; Cossi, M.; Millam, J. M.; Klene, M.; Adamo, C.; Cammi, R.; Ochterski, J. W.; Martin, R. L.; Morokuma, K.; Farkas, O.; Foresman, J. B.; Fox, D. J. *Gaussian 16*, revision C.01; Gaussian, Inc.: Wallingford, CT, 2016.

(25) Grimme, S. Supramolecular binding thermodynamics by dispersion-corrected density functional theory. *Chem. - Eur. J.* **2012**, *18*, 9955−9964.

(26) Funes-Ardoiz, I.; Paton, R. S. *GoodVibes*, v2.0.3, 2018.

(27) Because we cannot locate the binuclear $CO_2$ insertion transition state after multiple attempts, we used the highest energy point along the scanned reaction coordinate to estimate the energy of **TS2** (see Supporting Information section 6 for details).

(28) Marenich, A. V.; Jerome, S. V.; Cramer, C. J.; Truhlar, D. G. Charge model 5: An extension of Hirshfeld population analysis for the accurate description of molecular interactions in gaseous and condensed phases. *J. Chem. Theory Comput.* **2012**, *8*, 527−541.

(29) Falivene, L.; Credendino, R.; Poater, A.; Petta, A.; Serra, L.; Oliva, R.; Scarano, V.; Cavallo, L. SambVca 2. A web tool for



https://dx.doi.org/10.1021/acscatal.0c02299
*ACS Catal.* 2020, 10, 8870−8879

analyzing catalytic pockets with topographic steric maps. *Organometallics* **2016**, *35*, 2286−2293.

(30) The %ee is calculated using the equation $\text{ee} = \frac{1 - e^{-\Delta\Delta G^{\ddagger}/RT}}{1 + e^{-\Delta\Delta G^{\ddagger}/RT}} \times 100$, which leads to a calculated %ee > 99% with $\Delta\Delta G^{\ddagger}$ = 5.4 kcal/mol at 298.15 K.



https://dx.doi.org/10.1021/acscatal.0c02299
*ACS Catal.* 2020, 10, 8870−8879